

Peng Hu, Xin Tong, Li Lin, and Lihong V. Wang, Fellow, IEEE

Abstract—Tomographic imaging modalities described by large system matrices. To improve the temporal resolution of functional imaging in tomography, sparse spatial sampling is often employed, which degrades the system matrix and introduces artifacts in reconstructed images. Various existing techniques improve the image quality without correcting the system matrix and have limitations. Here, we compress the system matrix to improve computational efficiency (e.g., 42 times) using singular value decomposition and fast Fourier transform. Enabled by the efficiency, we propose fast sparsely sampling functional imaging by incorporating a densely sampled prior image into the system matrix, which maintains the critical linearity while mitigating artifacts. We demonstrate the methods in 3D photoacoustic computed tomography with significantly improved image quality and clarify their applicability to X-ray CT and radial-sampling MRI due to the similarities in system matrices.

Index Terms—Tomographic imaging, photoacoustic computed tomography, system matrix compression, system matrix manipulation, sparsely sampling functional imaging

I. INTRODUCTION

Tomographic imaging modalities X-ray computed tomography (CT), magnetic resonance imaging (MRI), and photoacoustic computed tomography (PACT) produce cross-sectional images of tissue by detection of penetrating X-rays [1], nuclear-magnetic-resonance-induced radio waves [2], [3], and light-absorption-induced ultrasonic waves [4], respectively. Each modality with a certain setup is described by a system matrix [5]–[10].

Accurate image reconstruction poses requirements to the system matrix, which are often violated. For example, to achieve high temporal resolution for functional imaging, the spatial sampling density is often sacrificed, which introduces artifacts in the reconstructed image [11]–[13] and compromises the functional signal extraction.

Numerous methods have been proposed to compensate for system-matrix imperfections from image-domain [12], [14]-[21], signal-domain [22]–[28], and cross-domain [29]–[33] perspectives. However, due to the large size of each system matrix, these methods tend not to manipulate or correct the system matrix directly and have limitations. For sparse sampling functional imaging, traditional methods [12], [16], [17], [19]–[21], [26], [33] mitigate artifacts in images but their performances drop sharply as the sampling density reduces. Deep neural networks (DNNs) [18], [22], [23], [25], [29], [32], [34] show high performance in mitigating artifacts but tend to generate false image features when the sampling density is low, and they require imaging-modality- and device-dependent datasets, which are not always available. Moreover, most of the methods introduce nonlinearity while mitigating artifacts, which disrupts the functional signals that are often much weaker than background signals.

Here, we compress the system matrices using singular value decomposition (SVD) and fast Fourier transform (FFT), which enables efficient system matrix slicing and manipulation. For sparse sampling functional imaging, we manipulate the system matrix with a densely sampled prior image, which effectively reduces unknown variables in image reconstruction with sparse sampling. Special configurations in the method maintain linearity in image reconstruction while substantially mitigating artifacts, which is critical for weak functional signal extraction. The proposed system matrix compression and manipulation methods are applicable to CT, MRI, and PACT. Note that the system matrix compression's effect on CT is minor due to the matrix's explicit high sparsity [1]. Nevertheless, the system matrix manipulation facilitates functional imaging in all three modalities.

In this work, we use 3D PACT for demonstration due to its representatively large size in tomography: light-absorption-induced ultrasonic wave from every voxel in an image is detected by every transducer element and the system matrix is

Manuscript received XX XX, 2025; accepted XX XX, 2025. This work was supported by National Institutes of Health grants U01 EB029823 (BRAIN Initiative), R35 CA220436 (Outstanding Investigator Award), and R01 CA282505. Lihong V. Wang has financial interests in Microphotoacoustics, Inc., CalPACT, LLC, and Union Photoacoustic Technologies, Ltd., which, however, did not support this work. (Corresponding author: Lihong V. Wang.)

This research involved animals. The animal experiments followed the protocol approved by the Institutional Animal Care and Use Committee of the California Institute of Technology.

Peng Hu, Xin Tong, and Lihong V. Wang are with the Caltech Optical Imaging Laboratory, Andrew and Peggy Cherng Department of Medical Engineering, Department of Electrical Engineering, California Institute of Technology, Pasadena, CA 91125 USA (e-mail: hupen0520@outlook.com; xtong2@caltech.edu; LVW@caltech.edu).

Li Lin was with the Caltech Optical Imaging Laboratory, Andrew and Peggy Cherng Department of Medical Engineering, Department of Electrical Engineering, California Institute of Technology, Pasadena, CA 91125 USA. He is currently with the College of Biomedical Engineering and Instrument Science, Zhejiang University, Hangzhou 310027, China (e-mail: linliokok@zju.edu.cn).

intrinsically a 6D tensor [10]. We apply the data-driven system matrix manipulation to both numerical simulations and *in vivo* mouse brain functional imaging with sparse sampling, and demonstrate that the method substantially improves the functional image accuracy.

Specifically, in Section II, we describe the forward operator in PACT and its compression in continuous form. In Section III. we simplify the forward operator expression for a flat rectangular transducer detection surface using the far-field approximation. Then, we discretize the forward operators into the system matrices in Section IV. Further, we introduce a hybrid method for image reconstruction based on system matrix manipulation (Section V) and a correlation-based method for functional signal extraction (Section VI), which enable our system for fast functional imaging. Next, we use numerical simulations to demonstrate the efficiency and accuracy of the compressed system matrix (Section VII), the high performance of the hybrid method in image reconstruction (Section VIII), and the effectiveness of the fast functional imaging method (Section IX). Finally, in Section X, we demonstrate the method's capability for fast mouse brain functional imaging in vivo.

II. FORWARD OPERATOR COMPRESSION IN PACT BASED ON SVD AND FFT

In an acoustically homogeneous medium, a photoacoustic wave can be expressed as [10], [35]

$$p(\mathbf{r},t) = \frac{1}{4\pi c^2} \int_{V} \frac{p_0(\mathbf{r}')}{\|\mathbf{r}' - \mathbf{r}\|} \frac{\partial}{\partial t} \delta\left(t - \frac{\|\mathbf{r}' - \mathbf{r}\|}{c}\right) d\mathbf{r}'.$$
 (1)

Here, $p(\mathbf{r}, t)$ is the pressure at location \mathbf{r} and time t, c is the speed of sound (SOS), V is the volumetric space occupied by the tissue, $p_0(\mathbf{r}')$ is the light-absorption-induced initial pressure at \mathbf{r}' , and $\delta(t)$ is the Dirac delta function. In this study, image reconstruction for PACT is to obtain $p_0(\mathbf{r}')$ from ultrasonic detections of $p(\mathbf{r}, t)$.

Assume that we have N finite-size ultrasonic transducer elements. For the n-th transducer element at \mathbf{r}_n with detection surface S_n , the average pressure on the detection surface at time t is expressed as

$$\tilde{p}(\mathbf{r}_n, t) = \frac{1}{A_n} \int_{\mathbf{r}_n} p(\mathbf{r}, t) da_n(\mathbf{r}).$$
 (2)

Here, A_n denotes the area of the surface S_n , and the Leibniz notation $da_n(\mathbf{r})$ represents the area of an infinitesimal subset of S_n around \mathbf{r} . We express the spatial impulse response (SIR) in Eq. (2) as [10]

$$h_{s,n}(\mathbf{r}',t) = \int_{S_m} \frac{\delta\left(t - \frac{\|\mathbf{r}' - \mathbf{r}\|}{c}\right)}{2\pi c \|\mathbf{r}' - \mathbf{r}\|} da_n(\mathbf{r}).$$
(3)

Then Eq. (2) becomes

$$\widetilde{p}(\mathbf{r}_{n},t) = \frac{1}{2c} \int_{V} p_{0}(\mathbf{r}') \frac{1}{A_{n}} \frac{\partial}{\partial t} \left[\int_{S_{n}} \frac{\delta\left(t - \frac{\|\mathbf{r}' - \mathbf{r}\|}{c}\right)}{2\pi c \|\mathbf{r}' - \mathbf{r}\|} da_{n}(\mathbf{r}) \right] d\mathbf{r}'$$

$$= \frac{1}{2c} \int_{V} p_{0}(\mathbf{r}') \frac{1}{A_{n}} \frac{\partial}{\partial t} h_{s,n}(\mathbf{r}',t) d\mathbf{r}'. \tag{4}$$

We denote the electric impulse response (EIR) of the n-th transducer as $h_{e,n}(t)$ and express the transducer's response using temporal convolution $*_t$ as

$$\hat{p}(\mathbf{r}_n, t) = \tilde{p}(\mathbf{r}_n, t) *_t h_{e,n}(t).$$
 (5)

Substituting Eq. (4) into Eq. (5) yields

$$\hat{p}(\mathbf{r}_{n},t) = \frac{1}{2c} \int_{V} p_{0}(\mathbf{r}') \frac{1}{A_{n}} \frac{\partial}{\partial t} h_{s,n}(\mathbf{r}',t) d\mathbf{r}' *_{t} h_{e,n}(t)$$

$$= \int_{V} p_{0}(\mathbf{r}') \frac{h'_{e,n}(t) *_{t} h_{s,n}(\mathbf{r}',t)}{2cA_{n}} d\mathbf{r}'$$

$$= \int_{V} p_{0}(\mathbf{r}') h_{n}(\mathbf{r}',t) d\mathbf{r}'.$$
(6)

Here, the prime in $h'_{e,n}(t)$ denotes the time derivative, and h_n denotes the point source response per unit initial pressure per unit infinitesimal tissue volume received by a finite-size transducer element:

$$h_n(\mathbf{r}',t) = \frac{h'_{e,n}(t) *_t h_{s,n}(\mathbf{r}',t)}{2cA_n}.$$
 (7)

Eq. (6) describes the forward operator in PACT that maps $p_0(\mathbf{r}')$ to $\hat{p}(\mathbf{r}_n, t)$, and the image reconstruction is to obtain $p_0(\mathbf{r}')$ from measurements of $\hat{p}(\mathbf{r}_n, t)$.

For convenience in the following discussion, we temporally shift $h_{s,n}(\mathbf{r}',t)$ and $h_n(\mathbf{r}',t)$ for \mathbf{r}' such that time 0 aligns with the onset of the nonzero signal received by the center of the *n*-th transducer element \mathbf{r}_n :

$$\hat{h}_{s,n}(\mathbf{r}',t) = h_{s,n} \left(\mathbf{r}', t + \frac{\|\mathbf{r}' - \mathbf{r}_n\|}{c} \right)$$

$$= \int_{S_n} \frac{\delta \left(t + \frac{\|\mathbf{r}' - \mathbf{r}_n\|}{c} - \frac{\|\mathbf{r}' - \mathbf{r}\|}{c} \right)}{2\pi c \|\mathbf{r}' - \mathbf{r}\|} da_n(\mathbf{r})$$
(8)

and

$$\hat{h}_{n}(\mathbf{r}',t) = h_{n} \left(\mathbf{r}', t + \frac{\|\mathbf{r}' - \mathbf{r}_{n}\|}{c} \right)$$

$$= \frac{h'_{e,n}(t) *_{t} h_{s,n} \left(\mathbf{r}', t + \frac{\|\mathbf{r}' - \mathbf{r}_{n}\|}{c} \right)}{2cA_{n}}$$

$$= \frac{h'_{e,n}(t) *_{t} \hat{h}_{s,n}(\mathbf{r}',t)}{2cA_{n}}.$$
(9)

Next, we express the SIR and point source response in the local coordinates of the transducer elements. In this study, we assume that the elements have the same EIR: $h_{e,n}(t) = h_e(t), n = 1,2,...,N$; and the measurement of $h_e(t)$ is discussed in the next section. We define the local coordinates of the n-th transducer element using its center location on the detection surface as the origin, the length direction as the x-axis, the width direction as the y-axis, and the normal direction (toward the detection region) as the z-axis. Here, we choose the x-axis and y-axis to let the coordinates satisfy the right-hand rule. We express the three axes of the local coordinates as three vectors of unit length: $\hat{\mathbf{x}}_n$, $\hat{\mathbf{y}}_n$, and $\hat{\mathbf{z}}_n$ (shown in Fig. 1a), which form an orthonormal matrix

$$\mathbf{A}_n = (\hat{\mathbf{x}}_n^{\mathrm{T}}, \hat{\mathbf{y}}_n^{\mathrm{T}}, \hat{\mathbf{z}}_n^{\mathrm{T}}). \tag{10}$$

Locations \mathbf{r}' , \mathbf{r}_n , and \mathbf{r} in the global coordinates correspond to the locations \mathbf{r}'_{lcl} , $\mathbf{0}$, and \mathbf{r}_{lcl} in the local coordinates of the *n*-th transducer element. Coordinate transformations yield $\mathbf{r}'_{lcl} = (\mathbf{r}' - \mathbf{r}_n)\mathbf{A}_n$ and $\mathbf{r}_{lcl} = (\mathbf{r} - \mathbf{r}_n)\mathbf{A}_n$. These global and local

coordinates satisfy $\|\mathbf{r}' - \mathbf{r}_n\| = \|\mathbf{r}'_{lcl}\|$ and $\|\mathbf{r}' - \mathbf{r}\| = \|\mathbf{r}'_{lcl}\|$ $\mathbf{r}_{\rm lcl}$ due to the orthonormality of the transformations. We denote the detection surface (S_n in the global coordinates) in the local coordinates as $S_{n,lcl}$, and denote the local Leibniz notation as $da_{n,lcl}(\mathbf{r}_{lcl}) = da_n(\mathbf{r})$. Thus, in the local coordinates of the n-th transducer element, we express Eq. (8) as

$$\hat{h}_{s,n}(\mathbf{r}',t) = \int_{S_{n,lcl}} \frac{\delta\left(t + \frac{\|\mathbf{r}'_{lcl}\|}{c} - \frac{\|\mathbf{r}'_{lcl} - \mathbf{r}_{lcl}\|}{c}\right)}{2\pi c \|\mathbf{r}'_{lcl} - \mathbf{r}_{lcl}\|} da_{n,lcl}(\mathbf{r}_{lcl}),$$

$$\mathbf{r}'_{lcl} = (\mathbf{r}' - \mathbf{r}_n)\mathbf{A}_{\mathbf{r}_n}, n = 1,2,...,N.$$
(11)

All transducer elements are geometrically identical and have the same local coordinates, meaning $S_{n,lcl} = S_{n',lcl}$ and $\mathrm{d}a_{n,\mathrm{lcl}}\left(\mathbf{r}_{\mathrm{lcl}}\right)=\mathrm{d}a_{n',\mathrm{lcl}}(\mathbf{r}_{\mathrm{lcl}})$ for $n,n'\in\{1,2,\ldots,N\}.$ We define $S_{lcl} = S_{1,lcl}$, $da_{lcl} (\mathbf{r}_{lcl}) = da_{1,lcl} (\mathbf{r}_{lcl})$, and rewrite Eq. (11) as

$$\hat{h}_{s,lcl}(\mathbf{r}'_{lcl},t) = \int_{\mathcal{S}_{lcl}} \frac{\delta\left(t + \frac{\|\mathbf{r}'_{lcl}\|_{cl}}{c} - \frac{\|\mathbf{r}'_{lcl} - \mathbf{r}_{lcl}\|_{cl}}{c}\right)}{2\pi c \|\mathbf{r}'_{lcl} - \mathbf{r}_{lcl}\|_{cl}} da_{lcl}(\mathbf{r}_{lcl}), \quad (12)$$
which is now independent of the transducer element index n .

Replacing $h'_{e,n}(t)$ and $\hat{h}_{s,n}(\mathbf{r}',t)$ with $h'_{e}(t)$ and $\hat{h}_{s,lcl}(\mathbf{r}'_{lcl},t)$, respectively, in Eq. (9), we define

$$\hat{h}_{lcl}(\mathbf{r}'_{lcl}, t) = \frac{h'_{e}(t) *_{t} \hat{h}_{s,lcl}(\mathbf{r}'_{lcl}, t)}{2cA_{n}}.$$
(13)

Thus, we need to calculate only the values of $\hat{h}_{\rm s,lcl}({\bf r}_{\rm lcl}',t)$ and $\hat{h}_{lcl}(\mathbf{r}'_{lcl},t)$, then obtain the values of $\hat{h}_{s,n}(\mathbf{r}',t)$ and $\hat{h}_{n}(\mathbf{r}',t)$ through coordinate transformation:

$$\hat{h}_{s,n}(\mathbf{r}',t) = \hat{h}_{s,lcl}(\mathbf{r}'_{lcl},t) \tag{14}$$

and

$$\hat{h}_{n}(\mathbf{r}',t) = \frac{h'_{e,n}(t) *_{t} \hat{h}_{s,n}(\mathbf{r}',t)}{2cA_{n}}$$

$$= \frac{h'_{e}(t) *_{t} \hat{h}_{s,lcl}(\mathbf{r}'_{lcl},t)}{2cA_{n}} = \hat{h}_{lcl}(\mathbf{r}'_{lcl},t), \tag{15}$$

 $= \frac{h'_{\rm e}(t) *_{t} \hat{h}_{\rm s,lcl}(\mathbf{r}'_{\rm lcl},t)}{2cA_{n}} = \hat{h}_{\rm lcl}(\mathbf{r}'_{\rm lcl},t), \tag{15}$ respectively, with $\mathbf{r}'_{\rm lcl} = (\mathbf{r}' - \mathbf{r}_{n})\mathbf{A}_{n}$ for n = 1,2,...,N. Through these relations, we express both the SIR and the point source response in the local coordinates.

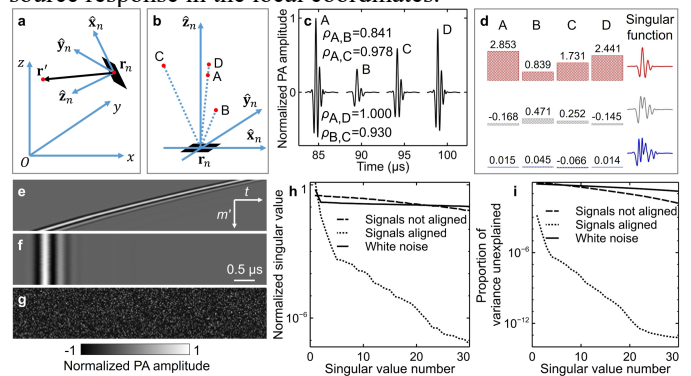


Fig. 1 Compression of the forward operator based on SVD. a A point source (a red dot), the n-th transducer element (a black rectangular centered at \mathbf{r}_n), and the element's local coordinate system with axes $\hat{\mathbf{x}}_n$, $\hat{\mathbf{y}}_n$, and $\hat{\mathbf{z}}_n$. b Four point sources A, B, C, and D (red dots) in the local coordinate system of the n-th transducer element. Points A, D, and \mathbf{r}_n are on the same line. \mathbf{c} The responses of the transducer element to the signals from the four point sources and the PCC between every two responses. d Expression of the four responses using linear combinations (coefficients visualized with bars) of three temporal singular functions shown as red, gray, and blue curves, respectively, based on SVD. e-f Independent responses (e) of a transducer element to 50 point sources (index m' = 1, 2, ..., 50) with decreasing distances to the element, and the temporallyshifted form (f), which aligns the nonzero signals in time. g White-noise

responses of the same size as those in e and f. h-i Normalized singular values and proportions of the variances unexplained, respectively, in the SVDs of the signals in e, f, and g.

We visualize the signals detected by a transducer element by picking four point sources, labeled as A, B, C, and D, respectively, in the local coordinate system of the n-th transducer element (Fig. 1b), with points A, D, and the element center \mathbf{r}_n on the same line. The element's responses to the signals from the point sources are shown in Fig. 1c. We let $\rho_{A,B}$ denote the Pearson correlation coefficient (PCC) between the responses corresponding to A and B. A direct implementation of the forward operator based on Eq. (6) is computationally intensive. Although $\rho_{A,D} = 1$, due to the effects of SIR, $\rho_{A,B}$, $\rho_{A,C}$, and $\rho_{B,C}$ are less than 1, indicating the signals from points A, B, and C are not shift-invariant; thus, an efficient temporal convolution with one kernel function cannot yield the detected signals accurately.

To accelerate the forward operator, we decouple the spatial and temporal dimensions of $\hat{h}_{lcl}(\mathbf{r}'_{lcl},t)$ using SVD while keeping only the dominant components:

$$\hat{h}_{\mathrm{lcl}}(\mathbf{r}_{\mathrm{lcl}}',t) \approx \sum_{k=1}^{K} \hat{h}_{\mathrm{lcl},k}(\mathbf{r}_{\mathrm{lcl}}')\eta_{k}(t). \tag{16}$$

Here, $\hat{h}_{lcl,k}(\mathbf{r}'_{lcl})$ and η_k denote the k-th spatial singular function and the k-th temporal singular function, respectively; and we use the first K terms to approximate the whole series. Combining Eqs. (9), (15), and (16), we obtain

$$h_{n}(\mathbf{r}',t) = \hat{h}_{n}\left(\mathbf{r}',t - \frac{\|\mathbf{r}' - \mathbf{r}_{n}\|}{c}\right)$$

$$= \hat{h}_{lcl}\left((\mathbf{r}' - \mathbf{r}_{n})\mathbf{A}_{n},t - \frac{\|\mathbf{r}' - \mathbf{r}_{n}\|}{c}\right)$$

$$\approx \sum_{k=1}^{K} \hat{h}_{lcl,k}\left((\mathbf{r}' - \mathbf{r}_{n})\mathbf{A}_{n}\right)\eta_{k}\left(t - \frac{\|\mathbf{r}' - \mathbf{r}_{n}\|}{c}\right). \tag{17}$$

Substituting Eq. (17) into Eq. (6), we obtain

$$\hat{p}(\mathbf{r}_{n},t) \approx \int_{V} p_{0}(\mathbf{r}') \sum_{k=1}^{K} \hat{h}_{\mathrm{lcl},k} ((\mathbf{r}' - \mathbf{r}_{n}) \mathbf{A}_{n}) \eta_{k} \left(t - \frac{\|\mathbf{r}' - \mathbf{r}_{n}\|}{c} \right) d\mathbf{r}'$$

$$= \sum_{k=1}^{K} \eta_{k}(t) *_{t} \int_{V} p_{0}(\mathbf{r}') \hat{h}_{\mathrm{lcl},k} ((\mathbf{r}' - \mathbf{r}_{n}) \mathbf{A}_{n}) \delta \left(t - \frac{\|\mathbf{r}' - \mathbf{r}_{n}\|}{c} \right) d\mathbf{r}',$$

$$n = 1.2 \quad N_{t} > 0.$$
(18)

As shown in this equation, we split the temporal variable from the spatial integrals, which allows for a fast implementation of the forward operator.

We apply Eq. (16) with K = 3 to the responses in Fig. 1c for an initial demonstration. The three temporal singular functions $\eta_1(t)$, $\eta_2(t)$, $\eta_3(t)$ are shown as red, gray, and blue curves, respectively, in Fig. 1d, and the values of spatial singular functions are visualized as bars. Then we explain the necessity of temporal shifting for alignment, described in Eqs. (8) and (9), for SVD. We select 50 point sources with decreasing distances to a transducer element and visualize the element's independent responses to them in Fig. 1e. The temporallyshifted form of these responses based on Eq. (9) is shown in **Fig. 1f.** We also add white-noise responses with the same size for comparison, as shown in Fig. 1g. Performing SVD to the three sets of responses, we observe different compression efficiencies from the perspectives of normalized singular value

(**Fig. 1h**) and proportion of the variance (**Fig. 1i**). In both figures, we see that the compression efficiency of the original responses is similar to that of the white-noise responses, whereas the efficiency for the temporally-shifted responses is significantly higher (necessary for the compression).

III. POINT SOURCE RESPONSE OF AN ULTRASONIC TRANSDUCER WITH A FLAT RECTANGULAR DETECTION SURFACE

The fast forward operator can be configured for a transducer with any detection surface. Here, we only discuss an ultrasonic transducer with a flat rectangular detection surface with a length a of 0.7 mm and a width b of 0.6 mm, which is used in our 3D imaging system [36]. We see from Eqs. (6) and (15) that the forward operator is based on the point source response $\hat{h}_{lcl}(\mathbf{r}'_{lcl},t)$ in the local coordinates. The response is determined by the first derivative of EIR $(h'_e(t))$ and the realigned SIR $(\hat{h}'_{s,lcl}(\mathbf{r}'_{lcl},t))$ in the local coordinates. In general, we can measure $\hat{h}_{lcl}(\mathbf{r}'_{lcl},t)$ experimentally. In this research, for an ultrasonic transducer with a flat rectangular detection surface, we calculate $\hat{h}_{lcl}(\mathbf{r}'_{lcl},t)$ efficiently using the far-field approximation of $\hat{h}_{s,lcl}(\mathbf{r}'_{lcl},t)$ [10]. From a special case of this approximation, we derive a method to measure $h'_e(t)$ experimentally.

In the first step of obtaining $\hat{h}_{lcl}(\mathbf{r}'_{lcl},t)$, we introduce the calculation of $\hat{h}_{lcl}(\mathbf{r}'_{lcl},t)$ based on the far-field approximation of $\hat{h}_{s,lcl}(\mathbf{r}'_{lcl},t)$. In this research, the image domain is within the far-field regions of all transducer elements. Using the far-field approximation, we express the SIR in the frequency domain as [10]

$$F_{t}\left(h_{s,n}(\mathbf{r}',t)\right)(f) \approx \frac{ab \exp\left(-j2\pi f \frac{\|\mathbf{r}'-\mathbf{r}_{n}\|}{c}\right)}{2\pi c \|\mathbf{r}'-\mathbf{r}_{n}\|}$$
$$\operatorname{sinc}\left(\pi f \frac{a|(\mathbf{r}'-\mathbf{r}_{n})\hat{\mathbf{x}}_{n}^{\mathrm{T}}|}{c \|\mathbf{r}'-\mathbf{r}_{n}\|}\right) \operatorname{sinc}\left(\pi f \frac{b|(\mathbf{r}'-\mathbf{r}_{n})\hat{\mathbf{y}}_{n}^{\mathrm{T}}|}{c \|\mathbf{r}'-\mathbf{r}_{n}\|}\right). \tag{19}$$

Here, F_t denotes the temporal Fourier transform (FT), and j denotes the imaginary unit. Combining Eqs. (14) and (19), we apply the temporal FT to $\hat{h}_{\text{S,lcl}}(\mathbf{r}'_{\text{lcl}},t)$ and obtain

$$F_{t}\left(\hat{h}_{s,lcl}(\mathbf{r}'_{lcl},t)\right)(f) = F_{t}\left(h_{s,n}\left(\mathbf{r}',t + \frac{\|\mathbf{r}' - \mathbf{r}_{n}\|}{c}\right)\right)(f)$$

$$= \exp\left(j2\pi f \frac{\|\mathbf{r}' - \mathbf{r}_{n}\|}{c}\right)F_{t}\left(h_{s,n}(\mathbf{r}',t)\right)(f)$$

$$\approx \frac{ab}{2\pi c\|\mathbf{r}' - \mathbf{r}_{n}\|}\operatorname{sinc}\left(\pi f \frac{a|(\mathbf{r}' - \mathbf{r}_{n})\hat{\mathbf{x}}_{n}^{\mathrm{T}}|}{c\|\mathbf{r}' - \mathbf{r}_{n}\|}\right)\operatorname{sinc}\left(\pi f \frac{b|(\mathbf{r}' - \mathbf{r}_{n})\hat{\mathbf{y}}_{n}^{\mathrm{T}}|}{c\|\mathbf{r}' - \mathbf{r}_{n}\|}\right)$$

$$= \frac{ab}{2\pi c\|\mathbf{r}'_{lcl}\|}\operatorname{sinc}\left(\pi f \frac{a|\mathbf{x}'_{lcl}|}{c\|\mathbf{r}'_{lcl}\|}\right)\operatorname{sinc}\left(\pi f \frac{b|\mathbf{y}'_{lcl}|}{c\|\mathbf{r}'_{lcl}\|}\right). \tag{20}$$
Here, we use identities $\mathbf{r}'_{lcl} = (\mathbf{r}' - \mathbf{r}_{n})\mathbf{A}_{n} = (\mathbf{r}' - \mathbf{r}_{n})(\hat{\mathbf{x}}_{n}^{\mathrm{T}}, \hat{\mathbf{y}}_{n}^{\mathrm{T}}, \hat{\mathbf{z}}_{n}^{\mathrm{T}}) = (x'_{lcl}, y'_{lcl}, z'_{lcl}) \text{ and } \|\mathbf{r}' - \mathbf{r}_{n}\| = \|\mathbf{r}'_{lcl}\|, \text{ and } \mathbf{r}'_{lcl} \text{ must not be the origin in the local coordinates. Substituting Eq. (20) into the temporal FT of Eq. (13), we obtain$

$$F_{t}\left(\hat{h}_{lcl}(\mathbf{r}_{lcl}',t)\right)(f) = \frac{1}{2cab}F_{t}\left(h_{e}'(t)\right)(f)F_{t}\left(\hat{h}_{s,lcl}(\mathbf{r}_{lcl}',t)\right)(f)$$

$$\approx \frac{F_{t}\left(h_{e}'(t)\right)(f)}{4\pi c^{2}\|\mathbf{r}_{lcl}'\|}\operatorname{sinc}\left(\pi f \frac{a|x_{lcl}'|}{c\|\mathbf{r}_{lcl}'\|}\right)\operatorname{sinc}\left(\pi f \frac{b|y_{lcl}'|}{c\|\mathbf{r}_{lcl}'\|}\right). \tag{21}$$

Applying the temporal inverse FT to Eq. (21), we obtain $\hat{h}_{1:2}(\mathbf{r}'_{1:1},t) \approx$

$$F_t^{-1}\left(\frac{F_t(h'_e(t))(f)}{4\pi c^2 \|\mathbf{r}'_{lcl}\|} \operatorname{sinc}\left(\pi f \frac{a|x'_{lcl}|}{c \|\mathbf{r}'_{lcl}\|}\right) \operatorname{sinc}\left(\pi f \frac{b|y'_{lcl}|}{c \|\mathbf{r}'_{lcl}\|}\right)\right). \tag{22}$$

In the second step of obtaining $\hat{h}_{lcl}(\mathbf{r}'_{lcl}, t)$, we derive a method to measure $h'_{e}(t)$ by analyzing a special case of Eq. (22). We constrain the location \mathbf{r}'_{lcl} on the axis of the transducer by letting $\mathbf{r}'_{lcl} = (0,0,z'_{lcl})$, which simplifies Eq. (22) to

$$\hat{h}_{\rm lcl}(\mathbf{r}'_{\rm lcl}, t) \approx F_t^{-1} \left(\frac{F_t(h'_{\rm e}(t))(f)}{4\pi c^2 |z'_{\rm lcl}|} \right) = \frac{h'_{\rm e}(t)}{4\pi c^2 |z'_{\rm lcl}|}.$$
 (23)

Solving for $h'_{e}(t)$ from Eq. (23), we obtain

$$h'_{e}(t) \approx 4\pi c^{2} |z'_{lcl}| \hat{h}_{lcl}(\mathbf{r}'_{lcl}, t) = 4\pi c^{2} |z'_{lcl}| \hat{h}_{n}(\mathbf{r}', t)$$

$$= 4\pi c^{2} |z'_{lcl}| h_{n} \left((0, 0, z'_{lcl}) \mathbf{A}_{\mathbf{r}_{n}}^{-1} + \mathbf{r}_{n}, t + \frac{|z'_{lcl}|}{c} \right). \tag{24}$$

Here, we use the identity $\mathbf{r}' = \mathbf{r}'_{lcl} \mathbf{A}_n^{-1} + \mathbf{r}_n = (0,0,z'_{lcl}) \mathbf{A}_n^{-1} + \mathbf{r}_n$. In practice, we repeat the measurement of the right-hand side of Eq. (24) and use the average to represent $h'_e(t)$.

In summary, we measure $h'_{\rm e}(t)$ experimentally on the basis of Eq. (24) and substitute the measurement into Eq. (22) to obtain $\hat{h}_{\rm lcl}({\bf r}'_{\rm lcl},t)$. Further, we perform SVD to $\hat{h}_{\rm lcl}({\bf r}'_{\rm lcl},t)$ according to Eq. (16) and obtain singular functions $\hat{h}_{\rm lcl,k}({\bf r}'_{\rm lcl})$ and $\eta_k(t), k = 1,2,...,K$. We use these functions in Eq. (18) to implement the fast forward operator.

IV. DISCRETIZATION OF THE FORWARD OPERATOR

We express the forward operator in two different forms in Eqs. (6) and (18), respectively. First, we discretize the forward operator implemented in Eq. (6). In the temporal domain, we choose points of interest $t_l = t_1 + (l-1)\tau$, l = 1,2,...,L, where t_1 is the initial time, τ is the sampling step size, and L is the number of time points. Then we discretize the temporal FT of $h'_{\rm e}(t)$ as $F_t\big(h'_{\rm e}(t)\big)_{l'}\approx F_l(h'_l)(l'), l'=1,2,...,L$, where we define $h'_l=h'_{\rm e}(t_l)$, $F_t\big(h'_{\rm e}(t)\big)_{l'}=F_t\big(h'_{\rm e}(t)\big)(f_{l'})$, $l,l'\in\{1,2,...,L\}$, and let F_l represent the discrete FT with respect to l. The temporal frequencies $f_{l'},l'=1,2,...,L$ are selected according to the requirement of the discrete FT. We further denote the $m_{\rm lcl}$ -th location in the local coordinates as $\mathbf{r}'_{\rm lcl,m_{\rm lcl},l}=(x'_{\rm lcl,m_{\rm lcl}},y'_{\rm lcl,m_{\rm lcl}},z'_{\rm lcl,m_{\rm lcl}})$ and define $\hat{h}_{\rm lcl,m_{\rm lcl},l}=(\hat{h}_{\rm lcl}(\mathbf{r}'_{\rm lcl,m_{\rm lcl}},t_l),m_{\rm lcl}=1,2,...,M_{\rm lcl}$, where $M_{\rm lcl}$ is the number of locations of interest in the local coordinates. Thus, we discretize Eq. (22) as

$$\widehat{h}_{lcl,m_{lcl},l} \approx \frac{1}{4\pi c^{2} \|\mathbf{r}'_{lcl,m_{lcl}}\|} F_{l}(h'_{l})(l')
\times \operatorname{sinc}\left(\pi f_{l'} \frac{a |x'_{lcl,m_{lcl}}|}{c \|\mathbf{r}'_{lcl,m_{lcl}}\|}\right) \operatorname{sinc}\left(\pi f_{l'} \frac{b |y'_{lcl,m_{lcl}}|}{c \|\mathbf{r}'_{lcl,m_{lcl}}\|}\right) (l),
m_{lcl} = 1, 2, ..., M_{lcl}, l = 1, 2, ..., L.$$
(25)

Further, we discretize the point source response $h_n(\mathbf{r}',t)$ as $h_{n,m,l} = h_n(\mathbf{r}'_m,t_l), n = 1,2,...,N, m = 1,2,...,M, l = 1,2,...,L$. Here, M is the number of voxels (source points) in the image domain. On the basis of the relation $h_n(\mathbf{r}'_m,t_l)$ =

$$\hat{h}_n\left(\mathbf{r}_m',t_l-\frac{\|\mathbf{r}_m'-\mathbf{r}_n\|}{c}\right)=\hat{h}_{\mathrm{lcl}}\left((\mathbf{r}_m'-\mathbf{r}_n)\mathbf{A}_n,t_l-\frac{\|\mathbf{r}_m'-\mathbf{r}_n\|}{c}\right),\quad \text{we}$$

obtain the values of $h_{n,m,l}$ through spatiotemporal interpolation of the values of $\hat{h}_{lcl,m_{lcl},l}$. Denoting $\hat{p}_{n,l} = \hat{p}(\mathbf{r}_n, t_l)$ and $p_{0,m} = p_0(\mathbf{r}'_m)$, we discretize Eq. (6) as

$$\hat{p}_{n,l}^{\text{slow}} = \sum_{m=1}^{M} v_m h_{n,m,l} p_{0,m}, n = 1, 2, ..., N, l = 1, 2, ..., L.$$
 (26)

Here, $\hat{p}_{n,l}^{\text{slow}}$ represents an approximation of $\hat{p}_{n,l}$ using this relatively slow forward operator, and v_m represents the volume of the m-th voxel. In practice, due to the finite duration of every point source response (shown in **Fig. 1c**, **e**, and **f**), given a combination of m and n, we need to calculate only for l in a range of length l' < l. Here, l' is the effective length for nonzero values in the discretized point source responses, and the computational complexity of the discrete forward operator in Eq. (26) is O(NML').

Next, we discretize the forward operator to a form with lower computational complexity from Eq. (18). We denote $\bar{h}_{lcl,k,m_{lcl}} = \hat{h}_{lcl,k}(\mathbf{r}'_{lcl,m_{lcl}})$ and $\eta_{k,l} = \eta_k(t_l)$, k = 1,2,...,K, $m_{lcl} = 1,2,...,M_{lcl}$, l = 1,2,...,L. After obtaining the array $\hat{h}_{lcl,m_{lcl},l}$ through Eq. (25), we estimate $\bar{h}_{lcl,k,m_{lcl}}$ and $\eta_{k,l}$ through SVD:

$$\hat{h}_{\text{lcl},m_{\text{lcl}},l} \approx \sum_{k=1}^{K} \bar{h}_{\text{lcl},k,m_{\text{lcl}}} \eta_{k,l},$$

$$\eta_{\text{lcl}} = 1, 2, ..., M_{\text{lcl}}, l = 1, 2, ..., L.$$
(27)

 $m_{\rm lcl} = 1, 2, ..., M_{\rm lcl}, l = 1, 2, ..., L. \tag{27}$ We denote $\hat{h}_{{\rm lcl},k,n,m} = \hat{h}_{{\rm lcl},k} ((\mathbf{r}'_m - \mathbf{r}_n) \mathbf{A}_n)$, which is obtained from the values of $\bar{h}_{{\rm lcl},k,m_{\rm lcl}}$ through spatial interpolation.

Moreover, we express
$$\delta\left(t - \frac{\|\mathbf{r}' - \mathbf{r}_n\|}{c}\right)$$
 in the discrete form as

$$\frac{1}{\tau} \left(\left(t_{l_{n,m}+1} - \frac{\|\mathbf{r}_m' - \mathbf{r}_n\|}{c} \right) \delta_{l,l_{n,m}} + \left(\frac{\|\mathbf{r}_m' - \mathbf{r}_n\|}{c} - t_{l_{n,m}} \right) \delta_{l,l_{n,m}+1} \right),$$

 $n=1,2,...,N, m=1,2,...,M, l=1,2,...,L. \qquad (28$ Here, $l_{n,m}$ denotes the temporal index such that $t_{l_{n,m}} \leq \|\mathbf{r}'_{n,m} - \mathbf{r}_{n}\|$

 $\frac{\|\mathbf{r}_{m}'-\mathbf{r}_{n}\|}{c} < t_{l_{n,m+1}}$, and we use the Kronecker delta function

$$\delta_{l,l'} = \begin{cases} 0, l \neq l', \\ 1, l = l'. \end{cases}$$
 (29)

We discretize the forward operator in Eq. (18) as

$$\sum_{k=1}^{K} \eta_{k,l} *_{l} \sum_{m=1}^{M} v_{m} \hat{h}_{lcl,k,n,m} p_{0,m} \frac{1}{\tau} \begin{bmatrix} \left(t_{l_{n,m}+1} - \frac{\|\mathbf{r}'_{m} - \mathbf{r}_{n}\|}{c} \right) \delta_{l,l_{n,m}} \\ + \left(\frac{\|\mathbf{r}'_{m} - \mathbf{r}_{n}\|}{c} - t_{l_{n,m}} \right) \delta_{l,l_{n,m}+1} \end{bmatrix},$$

$$n = 1, 2, ..., N, l = 1, 2, ..., L. \tag{30}$$

Here, $\hat{p}_{n,l}^{\text{fast}}$ represents an approximation of $\hat{p}_{n,l}$ using the fast forward operator, and $*_l$ denotes the discrete convolution with respect to l. In practice, we choose a value of L so that $\log_2 L$ is an integer, and we implement the discrete convolution using the temporal FFT. Thus, the computational complexity of the discrete forward operator in Eq. (30) is $O(NMK) + O(N(L\log_2 L)K)$.

The big O notations for both operators mean that there exist constants β_1 , β_2 , and β_3 (all independent from N, M, L, L', and K) such that the computations based on the slow and fast

forward operators, respectively, can be done in times less than $\beta_1 NML'$ and $\beta_2 NMK + \beta_3 N(L\log_2 L)K$. The slow forward operator consists of only spatial integration; whereas, the fast forward operator consists of two layers of operations, and the terms $\beta_2 NMK$ and $\beta_3 N(L\log_2 L)K$ are responsible for the inner layer spatial integration with $\hat{h}_{\text{lcl},k,n,m}$ and the outer layer temporal convolution with $\eta_{k,l}$, respectively.

V. A HYBRID METHOD FOR IMAGE RECONSTRUCTION FROM SPARSELY SAMPLED RAW DATA AND A PRIOR IMAGE

We first acquire signals from an object with transducers at enough locations (N, dense sampling). Then we continuously acquire multiple sets of signals from the object with transducers at a smaller number of locations (N', sparse sampling) for fast functional imaging. We assume that the object does not move as a whole during functional imaging.

For image reconstruction, we denote the densely sampled signals and a set of sparsely sampled signals as $\hat{\mathbf{p}}_{NL\times 1}$ and $\hat{\mathbf{p}}_{N'L\times 1}^{s}$, respectively. We first obtain an image $\hat{\mathbf{p}}_{0,M\times 1}$ from the densely sampled signals $\hat{\mathbf{p}}_{NL\times 1}$ by solving the regularized optimization problem

 $\begin{aligned} \mathbf{p}_{0,M\times 1} &= \\ \underset{\mathbf{p}_{0,M\times 1} \in \mathbb{R}^M, \mathbf{p}_{0,M\times 1} \geq \mathbf{0}}{\operatorname{argmin}} \left(\gamma_c \left\| \mathbf{H}_{NL\times M} \mathbf{p}_{0,M\times 1} - \widehat{\mathbf{p}}_{NL\times 1} \right\|^2 + \lambda \left| \mathbf{p}_{0,M\times 1} \right|_{\mathrm{TV}} \right) (31) \\ \text{using a fast iterative shrinkage-thresholding algorithm (FISTA)} \\ \text{with a constant step size [37]. Here, } \gamma_c \text{ represents the system-specific measurement calibration factor, meaning } \gamma_c \widehat{\mathbf{p}}_{NL\times 1} \text{ is the reading of the data acquisition system; } \mathbf{H}_{NL\times M} \text{ is the dense-sampling system matrix; } \lambda \text{ means the regularization parameter;} \end{aligned}$

and $|\mathbf{p}_{0,M\times 1}|_{TV}$ denotes $\mathbf{p}_{0,M\times 1}$'s total variation (TV) norm,

 $\left|\mathbf{p}_{0,M\times1}\right|_{\text{TV}} = \sum_{\substack{2 \le m_1 \le M_1 \\ 2 \le m_2 \le M_2 \\ 2 \le m_3 \le M_3}} \left(\frac{\left(\frac{p_{0,m_1,m_2,m_3} - p_{0,m_1-1,m_2,m_3}}{v_{m,1}}\right)^2 + \left(\frac{p_{0,m_1,m_2,m_3} - p_{0,m_1,m_2-1,m_3}}{v_{m,2}}\right)^2 + . (32)}{\left(\frac{p_{0,m_1,m_2,m_3} - p_{0,m_1,m_2,m_3-1}}{v_{m,2}}\right)^2}\right)$

In this definition, $v_{m,1}$, $v_{m,2}$, and $v_{m,3}$ represent the voxel sizes along the x-axis, y-axis, and z-axis, respectively; M_1 , M_2 , and M_3 ($M = M_1 M_2 M_3$) denote the number of voxels in the first, second, and third dimensions, respectively; and we reshape the column vector $\mathbf{p}_{0,M\times 1}$ to a 3D array $\mathbf{p}_{0,M_1\times M_2\times M_3}$ with elements p_{0,m_1,m_2,m_3} to express 3D information, $m_1 = 1,2,\ldots,M_1,m_2 = 1,2,\ldots,M_2,m_3 = 1,2,\ldots,M_3$.

To obtain an image from $\hat{\mathbf{p}}_{N'L\times 1}^s$ directly, we can use $\hat{\mathbf{p}}_{N'L\times 1}^s$ and the sparse-sampling system matrix $\mathbf{H}_{N'L\times M}^s$ to replace $\hat{\mathbf{p}}_{NL\times 1}$ and $\mathbf{H}_{NL\times M}$, respectively, in Eq. (31) and solve the problem

problem
$$\widehat{\mathbf{p}}_{0,M\times 1}^{S} = \underset{\mathbf{p}_{0,M\times 1}^{S} \in \mathbb{R}^{M}, \mathbf{p}_{0,M\times 1}^{S} \geq \mathbf{0}}{\operatorname{argmin}} \left(\gamma_{c} \left\| \mathbf{H}_{N'L\times M}^{S} \mathbf{p}_{0,M\times 1}^{S} - \widehat{\mathbf{p}}_{N'L\times 1}^{S} \right\|^{2} + \lambda \left| \mathbf{p}_{0,M\times 1}^{S} \right|_{TV} \right) (33)$$

using FISTA with a constant step size [37]. However, the nonlinearity introduced by the nonnegativity constraint and TV regularization may disrupt the functional signals. To maintain the linearity under sparse sampling, we treat $\hat{\mathbf{p}}_{0,M\times 1}$ as a prior

defined as

image and apply a smooth modulation to it to extract the dominant sources of aliasing artifacts by solving the optimization problem

$$\widehat{\mu}_{0.M'\times 1} =$$

$$\underset{\boldsymbol{\mu}_{0,M'\times 1} \in \mathbb{R}^{M'}}{\operatorname{argmin}} \left\| \boldsymbol{H}_{N'L\times M}^{s} \left(\widehat{\boldsymbol{p}}_{0,M\times 1} \odot \left(\boldsymbol{U}_{M\times M'} \boldsymbol{\mu}_{0,M'\times 1} \right) \right) - \widehat{\boldsymbol{p}}_{N'L\times 1}^{s} \right\|^{2} (34)$$

using FISTA without regularization. Here, $\mu_{0,M'\times 1}$ is a modulation image in the form of a column vector of size M' = $M_1'M_2'M_3'$ ($\ll M$), the symbol \odot denotes the element-wise product, and $\mathbf{U}_{M\times M'}$ is an upsampling operator transferring $\mu_{0,M'\times 1}$ to a smooth modulation image in the column-vector form of size M. To implement $\mathbf{U}_{M\times M'}$, we reshape the vector $\mu_{0,M'\times 1}$ into a 3D array $\mu_{0,M'_1\times M'_2\times M'_3}$, apply trilinear interpolation to the 3D array to obtain $\mu_{0,M_1 \times M_2 \times M_3}$, and flatten it to obtain $\mathbf{U}_{M\times M'}\mathbf{\mu}_{0,M'\times 1}$. The array $\mathbf{\mu}_{0,M_1\times M_2\times M_3}$ is a smooth array determined only by M' independent values. Thus, the expression $\widehat{\mathbf{p}}_{0,M\times 1} \odot (\mathbf{U}_{M\times M'}\mathbf{\mu}_{0,M'\times 1})$ represents a smooth modulation of the prior image $\hat{\mathbf{p}}_{0,M\times 1}$. By solving the optimization problem in Eq. (34) we obtain $\widehat{\mu}_{0,M'\times 1}$ and represent the dominant sources causing aliasing artifacts by $\widehat{\mathbf{p}}_{0,M\times 1} \odot (\mathbf{U}_{M\times M'}\widehat{\mathbf{\mu}}_{0,M'\times 1})$, which correspond to the dominant signals causing aliasing artifacts $\mathbf{H}_{N'L\times M}^{s}\left(\widehat{\mathbf{p}}_{0,M\times 1}\odot\right)$

 $(\mathbf{U}_{M\times M'}\widehat{\mathbf{\mu}}_{0,M'\times 1})$). It needs to be noted that the implementation of the forward operator based on Eq. (30) allows for efficient slicing of the system matrix, such as the matrix $\mathbf{H}_{N'L\times M}^{s}$, a slicing with respect to transducer element indices. Also, for a given set of parameters in FISTA, the solution to Eq. (34), $\widehat{\boldsymbol{\mu}}_{0,M'\times 1}$, depends linearly on $\widehat{\boldsymbol{p}}_{N'L\times 1}^{s}$.

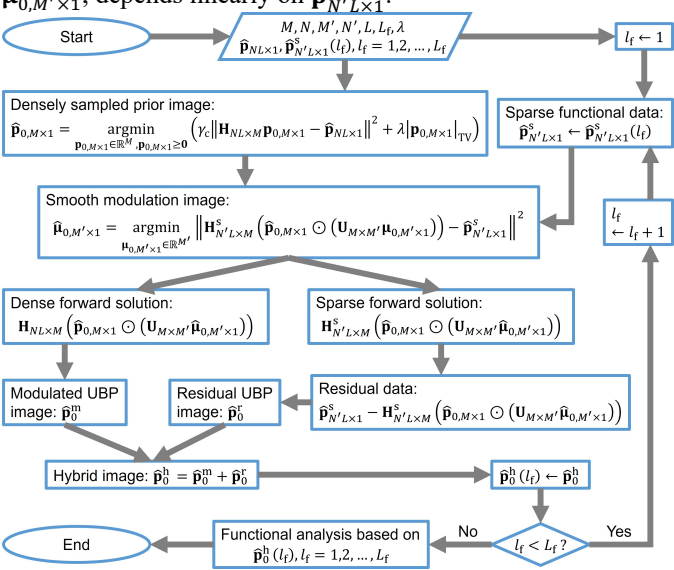


Fig. 2 Workflow of the hybrid method for image reconstruction from sparsely sampled raw data and a prior image.

Then, we apply the dense-sampling system matrix $\mathbf{H}_{NL\times M}$ to $\widehat{\mathbf{p}}_{0,M\times 1}\odot \left(\mathbf{U}_{M\times M'}\widehat{\mathbf{\mu}}_{0,M'\times 1}\right)$ to simulate the densely sampled signals $\mathbf{H}_{NL\times M}\left(\widehat{\mathbf{p}}_{0,M\times 1}\odot\left(\mathbf{U}_{M\times M'}\widehat{\boldsymbol{\mu}}_{0,M'\times 1}\right)\right)$, from which we use the universal back-projection (UBP) method [38] to reconstruct an image, denoted as $\hat{\mathbf{p}}_0^{\text{m}}$ (modulated UBP image). We further remove the aliasing artifacts caused by signals from $\widehat{\mathbf{p}}_{0,M\times 1} \odot (\mathbf{U}_{M\times M'}\widehat{\boldsymbol{\mu}}_{0,M'\times 1})$ by subtracting these signals from

obtain the residual $\widehat{\mathbf{p}}_{N'L\times 1}^{S}$ signals $\mathbf{H}_{N'L\times M}^{s}\left(\widehat{\mathbf{p}}_{0,M\times 1}\odot\left(\mathbf{U}_{M\times M'}\widehat{\mathbf{\mu}}_{0,M'\times 1}\right)\right)$ and using them with the UBP method to reconstruct an image, denoted as $\hat{\mathbf{p}}_0^r$ (residual UBP image). Due to the linearity of the UBP method, both images $\hat{\mathbf{p}}_0^{\mathrm{m}}$ and $\hat{\mathbf{p}}_0^{\mathrm{r}}$ are linearly dependent on $\hat{\boldsymbol{\mu}}_{0,M'\times 1}$ and thus on $\widehat{\mathbf{p}}_{N'L\times 1}^{s}$. We combine these two images to obtain the final

$$\widehat{\mathbf{p}}_0^{\mathsf{h}} = \widehat{\mathbf{p}}_0^{\mathsf{m}} + \widehat{\mathbf{p}}_0^{\mathsf{r}} \tag{35}$$

 $\widehat{\mathbf{p}}_0^h = \widehat{\mathbf{p}}_0^m + \widehat{\mathbf{p}}_0^r \tag{35}$ for $\widehat{\mathbf{p}}_{N'L\times 1}^s$. We summarize the workflow of the hybrid method in Fig. 2. We repeat the process for other sets of sparsely sampled raw data to obtain the images for further functional signal extraction.

Note that, an accurate reconstruction using UBP requires specific transducer array geometries, e.g., planar, spherical, and cylindrical surfaces [38], and artifacts occur when a hemispherical array is used in this study. However, these artifacts are negligible compared with those caused by sparse sampling, and the linearity of UBP is critical for the functional imaging discussed here. For simplicity, we use UBP in the hybrid method.

VI. CORRELATION-BASED FUNCTIONAL SIGNAL **EXTRACTION**

Given a set of reconstructed images $\hat{\mathbf{p}}_{0,l_f}$, $l_f=1,2,...,L_f$ in functional imaging, we propose a method to extract functional signals from them through regularized temporal correlation with a functional signal profile. To $\sup_{i} a_{j} = \sum_{j=1}^{J} a_{j}$, mean $a_{j} = \frac{\sup_{j} a_{j}}{J}$, and norm $a_{j} = \lim_{j \to \infty} a_{j} = \lim_{j \to \infty} a_{j}$ $\sum_{j=1}^{J} a_j^2$ for a series of numbers $a_j, j = 1, 2, ..., J$. We assume that the functional signal has a profile α_{f,l_f} , $l_f=1,2,...,L_f$ normalized to $\bar{\alpha}_{f,l_f} = \left(\alpha_{f,l_f} - \underset{l_f'}{\text{mean}} \alpha_{f,l_f'}\right) \left(\underset{l_f''}{\text{norm}} \left(\alpha_{f,l_f''} - \underset{l_f''}{\text{norm}} \right)\right)$ mean $\alpha_{\mathbf{f},l_{\mathbf{f}}'}$. The *m*-th voxel has a value of $\hat{p}_{0,l_{\mathbf{f}},m}$ in the $l_{\mathbf{f}}$ th image $\widehat{\mathbf{p}}_{0,l_{\mathrm{f}}}$. We can quantify the functional amplitude at the m-th voxel through the PCC between $\hat{p}_{0,l_{\mathrm{f}},m}$ and $\alpha_{\mathrm{f},l_{\mathrm{f}}}$:

which is not robust for very-low-amplitude regions. To improve the robustness, we add a regularization term to the denominator and obtain the regularized PCC (PCCR):

$$\begin{aligned} & \text{PCCR}_{\lambda_{f}}(\hat{p}_{0,l_{f},m},\alpha_{f,l_{f}}) = \\ & \frac{\sup_{l_{f}} \left(\bar{\alpha}_{f,l_{f}} \left(\hat{p}_{0,l_{f},m} - \max_{l_{f}'} \hat{p}_{0,l_{f}',m} \right) \right)}{\left(\underset{l_{f}}{\text{norm}} \left(\hat{p}_{0,l_{f},m} - \max_{l_{f}'} \hat{p}_{0,l_{f}',m} \right) \right) \\ + \lambda_{f} \max_{m'} \underset{l_{f}}{\text{norm}} \left(\hat{p}_{0,l_{f},m'} - \max_{l_{f}'} \hat{p}_{0,l_{f}',m'} \right) \right)} \\ & m = 1, 2, \dots, M. \end{aligned}$$

A 3D functional image is formed by assigning the regularized correlation to each voxel.

The assumed functional signal profile α_{f,l_f} is directly available in the numerical simulations (Eq. (43)). For mouse brain functional imaging *in vivo*, we obtain α_{f,l_f} through an initial UBP reconstruction, which is clarified in the section on *in vivo* study.

VII. EFFICIENCY AND ACCURACY OF THE FAST FORWARD OPERATOR

In this study, we used the 3D PACT system reported previously by Lin et al. [36], which consists of four 256-element arc transducer arrays (central frequency of 2.25 MHz and one-way bandwidth of 98%), and we assumed a homogeneous medium. In numerical simulations, we downsized each arc to 128 elements.

To quantify the efficiency and accuracy of the fast forward operator based on Eq. (30), we performed numerical simulations by placing a numerical phantom of size $1 \times 1 \times 1$ cm³ (**Fig. 3a**, with voxel values of 1 inside the solid and 0 elsewhere) in four image subdomains of the system $(D_1, D_2, D_3,$ and D_4 shown in **Fig. 3b**). The virtual 2D array formed by the rotation of the four arc arrays is marked by blue arcs and the rotation of the four subdomains around the same axis covers a domain (marked by black-dotted circles and arcs) enclosing all the image domains discussed in this study. We also implemented the slow forward operator according to Eq. (26) for comparison.

We first quantified the efficiency of the fast forward operator by performing forward simulations with the numerical phantom in the subdomain D_1 using both operators with parameters M = $50 \times 50 \times 50$ (voxel size of $0.2 \times 0.2 \times 0.2 \text{ mm}^3$), N = 396×128 (the four-arc array rotated for 99 locations and each arc downsized to 128 elements), L = 4096, L' = 151, and K =3. We ran the single-thread-CPU version (implemented in C++) of each operator 36 times on a server with Ubuntu 20.04.6 LTS and Intel(R) Xeon(R) Gold 6248R CPU @ 3.00GHz. Denoting the computation times of both operators as t_{fast} and t_{slow} , respectively, we obtained mean $(t_{\text{fast}}) = 6.3 \text{ min}$, $\text{std}(t_{\text{fast}}) =$ 0.4 min, $\text{mean}(t_{\text{slow}}) = 267 \text{ min}$, and $\text{std}(t_{\text{slow}}) = 19 \text{ min}$ for the 36 simulations and compared the values in Fig. 3c. Further, we performed a Welch's t-test between $42t_{fast}$ and t_{slow} , showing an insignificant difference (p-value = 0.59). Thus, the fast forward operator with K = 3 has approximately 42 times the speed of the slow forward operator. As K varies, the computation cost of the fast forward operator, O(NMK) + $O(N(L\log_2 L)K)$, is approximately proportional to K.

Note that the single-thread-CPU versions of the slow and fast forward operators were used here for a fair comparison of the operators' computation costs. In both operators, most of the computations are explicit matrix-vector multiplications and can be easily parallelized. Thus, for further image reconstructions, we implemented both operators in C++ and CUDA and used an NVIDIA A100 GPU for hardware acceleration. For the forward simulation of the subdomain D_1 , GPU acceleration reduced computation times of the fast and slow operators from 6.3 min and 267 min to 0.31 min and 10.2 min, respectively.

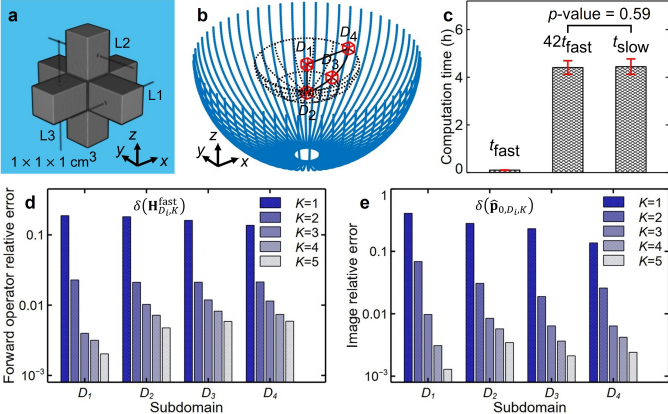


Fig. 3 Efficiency and accuracy of the fast forward operator. a A numerical phantom formed by three rectangular cuboids (each of size $2.6 \times 2.6 \times 10 \text{ mm}^3$) intersecting at their centers. Voxel values are 1 inside the phantom and 0 outside. Three lines (L1, L2, and L3) are picked for image-domain comparisons in Fig. 8 of Appendix A. b A virtual 2D array (blue-solid arcs), four subdomains of size $1 \times 1 \times 1 \text{ cm}^3 (D_1, D_2, D_3, \text{ and } D_4)$, and the domain occupied by rotations of the four subdomains around the array axis (black-dotted circles and arcs). c Computation times (t_{fast} and t_{slow}) of the fast and slow forward operators, respectively, for the forward simulations with the numerical phantom in D_1 (36 repetitions). d Relative error of the fast forward operator for subdomains D_1 , D_2 , D_3 , and D_4 , and for K = 1,2,3,4,5. e Relative error of the reconstructed image for the numerical phantom placed in subdomains D_1 , D_2 , D_3 , and D_4 , and for K = 1,2,3,4,5.

The accuracy of the fast forward operator is dependent on the value of K and we quantified this dependency by calculating the relative errors of the system matrix and the reconstructed image. For the numerical phantom (shown in **Fig. 3a**) placed in the subdomain D_i , we denote the ground truth image as \mathbf{p}_{0,D_i} , the ground-truth system matrix as $\mathbf{H}_{D_i}^{\text{slow}}$ (elements defined in Eq. (26)), and the system matrix compressed to the K-th singular function as $\mathbf{H}_{D_i,K}^{\text{fast}}$ (elements defined in Eq. (30)). Next, we define the system-matrix relative error as

we define the system-matrix relative error as
$$\delta(\mathbf{H}_{D_{i},K}^{\text{fast}}) = \frac{\left\|\mathbf{H}_{D_{i},K}^{\text{fast}} - \mathbf{H}_{D_{i}}^{\text{slow}}\right\|_{2}}{\left\|\mathbf{H}_{D_{i}}^{\text{slow}}\right\|_{2}}.$$
(38)

Here, we use the spectral norm of a matrix H,

$$\|\mathbf{H}\|_2 = \sqrt{\lambda_{\text{max}}(\mathbf{H}^{\text{T}}\mathbf{H})},\tag{39}$$

defined as the square root of the largest eigenvalue λ_{max} of the symmetric matrix $\mathbf{H}^T\mathbf{H}$, and \mathbf{H}^T means the transpose of \mathbf{H} . Then, we define the reconstructed-image relative error as

$$\delta(\widehat{\mathbf{p}}_{0,D_i,K}) = \frac{\|\widehat{\mathbf{p}}_{0,D_i,K} - \mathbf{p}_{0,D_i}\|}{\|\mathbf{p}_{0,D_i}\|},$$
(40)

with the image $\hat{\mathbf{p}}_{0,D_i,K}$ reconstructed by solving the optimization problem

$$\widehat{\mathbf{p}}_{0,D_i,K} = \underset{\mathbf{p}_0 \in \mathbb{R}^M, \mathbf{p}_0 \ge \mathbf{0}}{\operatorname{argmin}} \left\| \mathbf{H}_{D_i,K}^{\text{fast}} \mathbf{p}_0 - \mathbf{H}_{D_i}^{\text{slow}} \mathbf{p}_{0,D_i} \right\|^2$$
(41)

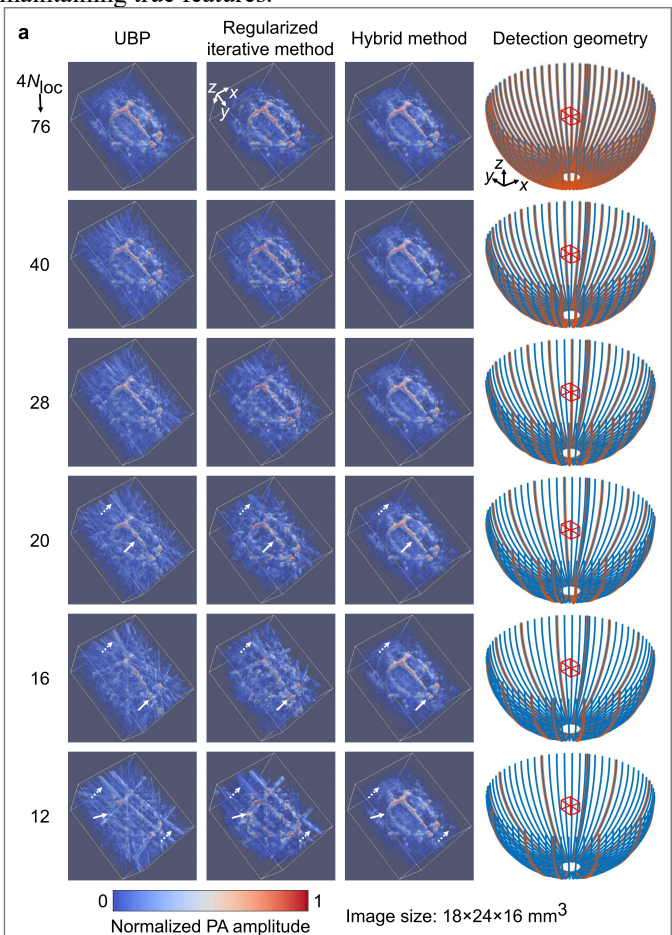
using FISTA with a nonnegativity constraint of the image.

For subdomains D_1 , D_2 , D_3 , and D_4 , and for K = 1,2,3,4,5, we performed power iterations to estimate each largest eigenvalue and calculated $\delta(\mathbf{H}_{D_i,K}^{\text{fast}})$, and we performed 256 FISTA iterations to obtain $\hat{\mathbf{p}}_{0,D_i,K}$ (intermediate results for K =3 shown in **Fig. 8** of Appendix A) and calculated $\delta(\widehat{\mathbf{p}}_{0,D_i,K})$. We compare the values of $\delta(\mathbf{H}_{D_i,K}^{\text{fast}})$ and $\delta(\widehat{\mathbf{p}}_{0,D_i,K})$ in Fig. 3d and e, respectively. When K = 3, the system-matrix relative error is below or very close to 1% for all subregions, and the reconstructed-image relative error is below 1% for all subregions. On the one hand, by changing K from 3 to 4, we observed negligible variations in the reconstructed structural and functional images in this study. On the other hand, changing K from 3 to 2 significantly increases the relative errors, e.g., a reconstructed-image relative error of 6.9% for D_1 , which has a risk of affecting certain regions of the image and compromising functional imaging. To achieve both high efficiency and high accuracy of the forward operator, we used K = 3 in this study.

Note that, for high interpretability of the intermediate results (**Fig. 8**), we used a simple numerical phantom for simulations in subdomains D_1 , D_2 , D_3 , and D_4 . More realistically, we designed two complex numerical phantoms with $M = 300 \times 300 \times 150$ (voxel size of $0.2 \times 0.2 \times 0.2$ mm³, shown in **Fig. 9a** and **b**, respectively, in Appendix B), performed simulations for both phantoms in a domain D (shown in **Fig. 9c**), and calculated the image relative error $\delta(\hat{\mathbf{p}}_{0,D,3})$ for the fast forward operator with K = 3. After 1280 FISTA iterations, the image relative error is 0.96% for phantom 1 and 0.78% for phantom 2 (both below 1%), which further demonstrates the high accuracy of the fast forward operator.

VIII. NUMERICAL SIMULATION OF THE HYBRID METHOD FOR IMAGE RECONSTRUCTION

We demonstrated the performance of the hybrid method by using it to reconstruct images from signals of a numerical phantom acquired by virtual arrays with different numbers of arcs: $4N_{loc} = 76, 40, 28, 20, 16, 12$. Here N_{loc} is the number of rotating locations of the four-arc array (with 128 transducer elements in each arc) in a virtual array. Images of the numerical phantom reconstructed using UBP, the regularized iterative method (Eq. (33)), and the hybrid method (Eq. (35) with a prior image obtained by performing a smooth modulation to the numerical phantom) are shown in the first three columns in **Fig.** 4a. The used virtual arrays are shown as blue arcs with red boundaries in the fourth column in Fig. 4a. We see that, as $4N_{loc}$ decreases from 76 to 12, the artifacts in the images reconstructed using UBP become more abundant. The regularized iterative method mitigates the relatively weak artifacts in all images but failed to suppress the strong artifacts such as in the images with $4N_{loc} = 16$, 12. In contrast, with the help of the prior image, the hybrid method significantly mitigates the artifacts. Quantitatively, for each method, we calculate the structural similarity index measures (SSIMs) between the images with $4N_{loc} = 40, 28, 20, 16, 12$ and that with $4N_{loc} = 76$, and compare the values in Fig. 4b. The hybrid method performs the best in mitigating artifacts and maintaining true features.



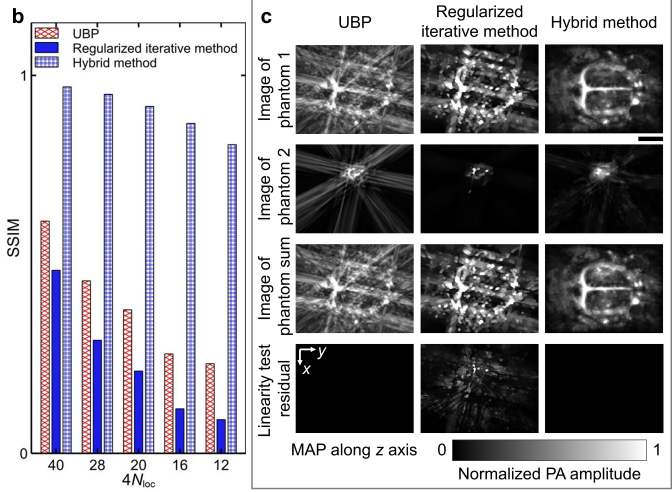


Fig. 4 UBP, regularized iterative method, and the proposed hybrid method for sparse-sampling imaging, and their linearity tests. **a** Images reconstructed by the three methods (first three columns) from signals detected at sparsely distributed elements (red-bounded blue curves in the fourth column) for $4N_{\rm loc} = 76, 40, 28, 20, 16, 12$. Examples of maintained features and suppressed artifacts are indicated by white-solid and white-dotted arrows, respectively. **b** SSIMs between the reconstructed images with $4N_{\rm loc} = 40, 28, 20, 16, 12$ and those with $4N_{\rm loc} = 76$ for the three methods. **c** Linearity tests of the three methods for $4N_{\rm loc} = 12$. Scale bar, 5 mm.

Additionally, we tested the linearity of each method by reconstructing two numerical phantoms and their summation. MAPs of the reconstructed images and the linearity test

residuals (image of the summation subtracted by images of the two phantoms) of the three methods with $4N_{loc} = 12$ are shown in **Fig. 4c**. The test validated that UBP and the hybrid method are linear, but the regularized iterative method is nonlinear. In the hybrid method, the prior image accuracy does not affect the linearity, but an inaccurate prior image may compromise the hybrid method's effectiveness in mitigating artifacts.

Due to the requirement of a prior image, the hybrid method's practical value mainly lies in fast functional imaging with sparse sampling, which is discussed in the next section.

IX. NUMERICAL SIMULATION OF THE HYBRID METHOD FOR FAST FUNCTIONAL IMAGING

We obtained numerical phantoms for functional imaging using

 $\mathbf{p}_{0,l_{\rm f}} = \alpha_{\rm b,l_{\rm f}} \mathbf{p}_{0,\rm b} + \alpha_{\rm f,l_{\rm f}} \mathbf{p}_{0,\rm f}, l_{\rm f} = 1,2,...,L_{\rm f}.$ (42) Here, $\mathbf{p}_{0,l_{\rm f}}$ is the $l_{\rm f}$ -th numerical phantom; $\mathbf{p}_{0,\rm b}$ (Fig. 5a, voxel size $0.1 \times 0.1 \times 0.1~\rm mm^3$) is the background phantom obtained in imaging with dense sampling and $\mathbf{p}_{0,\rm f}$ (Fig. 5b) is the functional phantom obtained by smoothing, downsampling, and zero padding of $\mathbf{p}_{0,\rm b}$; $\alpha_{\rm b,l_{\rm f}}$ and $\alpha_{\rm f,l_{\rm f}}$ are modulation factors of the two phantoms, respectively; and $L_{\rm f}$ is the number of numerical phantoms for functional imaging. The way $\mathbf{p}_{0,\rm b}$ is obtained guarantees that the mean value of nonzero voxels in $\mathbf{p}_{0,\rm b}$ approximately equals that in $\mathbf{p}_{0,\rm f}$. For simulations in this study, we used a virtual array formed by 12 arc arrays (Fig. 5c), let $L_{\rm f} = 36$, and let $\alpha_{\rm b,l_{\rm f}} \sim N(1,0.1)$, $l_{\rm f} = 1,2,...,L_{\rm f}$ (Fig. 5d), an amplitude similar to the image relative difference we observed

$$\alpha_{f,l_f} = \frac{A_f}{2} \left(\sin \frac{6\pi (l_f - 1)}{L_f} + 1 \right), l_f = 1, 2, \dots, L_f, \tag{43}$$

where $A_{\rm f}$ is the functional amplitude. The values of $\alpha_{\rm f,l_f}$ with $A_{\rm f}=0.18,0.06,0.02$ are shown in Fig. 5e and used in the simulations.

in mouse brain functional imaging. Also, we let

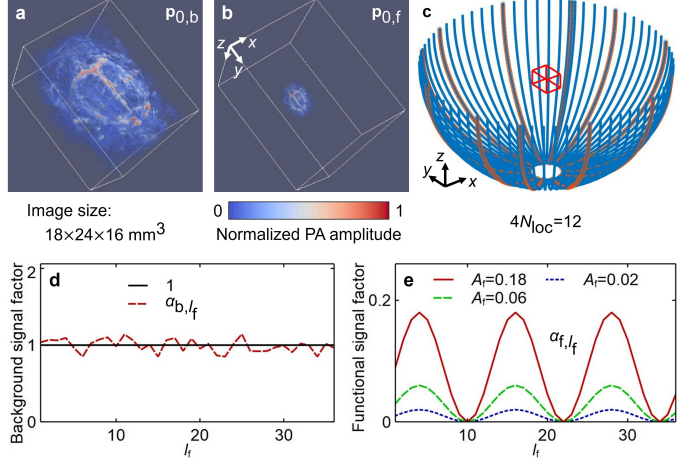


Fig. 5 Numerical phantoms for functional imaging. **a-b** The background and functional numerical phantoms, respectively, for functional imaging simulation. **c** A virtual array formed by 12 arc arrays, shown as arcs with red boundaries. **d-e** Modulation factors of the background and functional phantoms, respectively.

We performed forward simulations ($4N_{loc} = 12$), image reconstructions (UBP, the regularized iterative method in Eq. (33), and the hybrid method in Eq. (35)), and functional signal extractions (Eq. (37)) with different values of λ_f . The

functional images extracted from four sets of images (ground-truth images and images reconstructed with three methods) using the regularized-correlation-based method with $\lambda_f = 1.6$ are shown in Fig. 6 and Supplementary Video 1. We observe that artifacts in the UBP-reconstructed images cause artifacts in the functional images, the regularized iterative method mitigates artifacts in functional images but also compromises the true functional region, and the proposed hybrid has the best performance in functional imaging with sparse sampling. The results with other values of λ_f also support this observation.

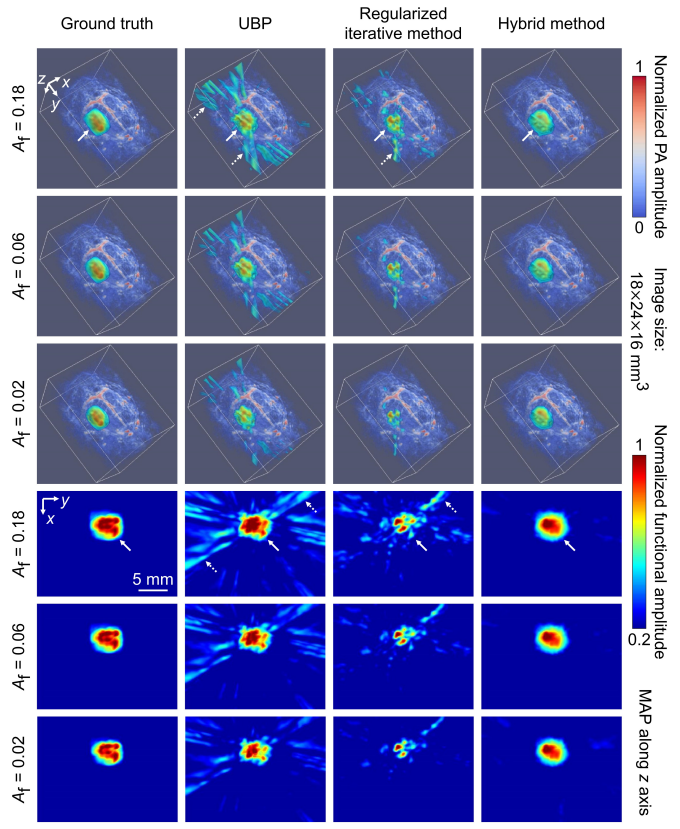


Fig. 6 Functional images extracted using the regularized-correlation-based method with $\lambda_{\rm f}=1.6$ from ground-truth images and images reconstructed with UBP, the regularized iterative method, and the hybrid method for $A_{\rm f}=0.18, 0.06, 0.02$. The first three rows show both the 3D functional and background images, and the last three rows show the MAPs of the functional images along the z-axis. In the first and fourth rows, the true functional regions and examples of false positive regions are indicated by white-solid and white-dotted arrows, respectively.

It needs to be noted that, in the hybrid method, both the modulated UBP image $\hat{\mathbf{p}}_0^m$ and the residual UBP image $\hat{\mathbf{p}}_0^r$ are linearly dependent on the sparsely sampled signals $\hat{\mathbf{p}}_{N'L\times 1}^s$. To visualize the functional signals in both $\hat{\mathbf{p}}_0^m$ and $\hat{\mathbf{p}}_0^r$, we apply the regularized-correlation-based method with $\lambda_f = 1.6$ to both sets of reconstructed images and compare them in **Fig. 10** (Appendix C) and **Supplementary Video 2**. We notice significant functional signals in both $\hat{\mathbf{p}}_0^m$ and $\hat{\mathbf{p}}_0^r$. On the one hand, functional regions obtained from $\hat{\mathbf{p}}_0^m$ (column 3 in **Fig. 10**) are much smaller than those from the ground truth images (column 1) and the hybrid images (column 2). In fact, reconstruction of the modulated UBP image $\hat{\mathbf{p}}_0^m$ is constrained by the prior image, which may break function signals in certain regions. On the other hand, functional images obtained from $\hat{\mathbf{p}}_0^r$ (column 4 in **Fig. 10**) show an elevated background after

normalization, which results in an enlarged true functional region and more false-positive regions. Thus, only the modulated UBP image $\hat{\mathbf{p}}_0^m$ or the residual UBP image $\hat{\mathbf{p}}_0^r$ is not sufficient in providing functional signals, and it is necessary to combine them $(\hat{\mathbf{p}}_0^h = \hat{\mathbf{p}}_0^m + \hat{\mathbf{p}}_0^r)$ for robust functional imaging.

X. MOUSE BRAIN FUNCTIONAL IMAGING IN VIVO

Finally, we applied UBP, the regularized iterative method, and the hybrid method to mouse brain functional imaging *in vivo* using the four-arc system. We first obtained a prior image of a mouse brain through dense sampling $(4N_{loc} = 396)$, then electrically stimulated its right front paw and continuously acquired signals from the mouse brain through sparse sampling $(4N_{loc} = 76, 2 \text{ s per image})$.

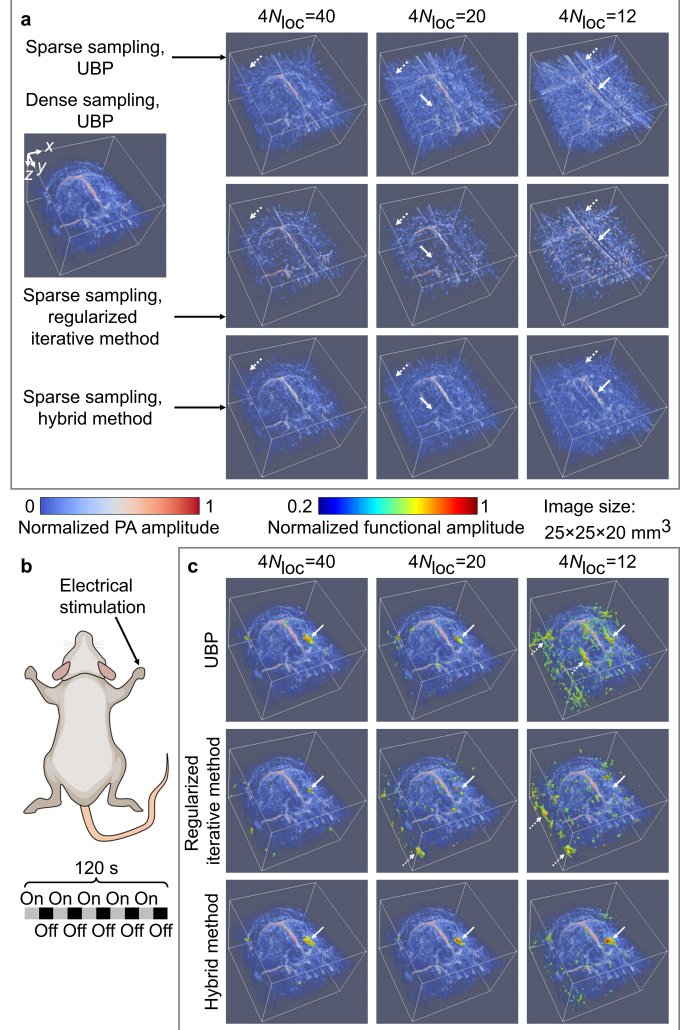


Fig. 7 Sparse-sampling mouse brain functional imaging *in vivo*. **a** A densely sampled image of a mouse brain reconstructed by UBP (left column, $4N_{loc} = 396$) and sparsely sampled images of the mouse brain reconstructed using UBP (first row), the regularized iterative method (second row), and the hybrid method (third row), respectively, for $4N_{loc} = 40, 20, 12$. Examples of suppressed artifacts and maintained features are indicated by white-dotted and white-solid arrows, respectively. **b** Electrical stimulation to the mouse's right front paw: five cycles, each with 12-s stimulation on and 12-s off. **c** Functional images obtained from the images reconstructed using UBP (first row, $\lambda_f = 0.32$), the regularized iterative method (second row, $\lambda_f = 0.08$), and the hybrid method (third row, $\lambda_f = 0.32$), respectively, for $4N_{loc} = 40, 20, 12$. The true functional regions in all images are indicated by white-solid arrows, and examples of false positive regions are indicated by white-dotted arrows.

To obtain the functional signal profile α_{f,l_f} , we first let it be a sinusoidal profile synchronized with the paw stimulation pattern and used it in the correlation-based method to obtain a functional image from UBP reconstructed images with $4N_{loc} = 76$. Then we identified a functional region from the functional image by thresholding using 90% of its maximum voxel value, calculated the mean value in this region for each UBP reconstructed image, and assigned the mean values to α_{f,l_f} , l_f =1,2,..., L_f .

We used subsets of the sparsely sampled signals $(4N_{loc} =$ 40, 20, 12) to demonstrate the performance of the hybrid method. For one set of sparsely sampled signals, the images reconstructed using UBP, the regularized iterative method, and the hybrid method for $4N_{loc} = 40, 20, 12$ are shown in Fig. 7a. We observe that the iterative method mitigates the artifacts (e.g., those indicated by white-dotted arrows) but compromises low-amplitude features (e.g., those indicated by white-solid arrows for $4N_{loc} = 20$). In contrast, the hybrid method maintains low-amplitude features while substantially mitigating the artifacts, resulting in images more similar to the densely sampled image. Electrical stimulation of the mouse's right front paw occurred in five cycles, each with 12-s stimulation on and 12-s off, as shown in Fig. 7b. We obtained functional images from the images reconstructed through the $4N_{\rm loc} = 40, 20, 12$ using $\lambda_{\rm f} =$ methods for 0.02, 0.08, 0.32, 1.28, 5.12, and observed that, for UBP and the hybrid method, $\lambda_f = 0.32$ was the best choice to maintain the true functional region and suppress false positive regions. For the regularized iterative method, $\lambda_f = 0.08$ was the best choice. We summarize the obtained functional images with the best values of λ_f in Fig. 7c and Supplementary Video 3. Results from UBP and the hybrid method match well for $4N_{loc} = 40$. The hybrid method is slightly (significantly) better than UBP for $4N_{loc} = 20$ ($4N_{loc} = 12$). Due to the violation of linearity, the regularized iterative method compromises the true functional region: leading to its shrinkage for $4N_{loc} = 40,20$ and its decimation altogether for $4N_{loc} = 12$. In summary, the proposed hybrid method enables fast functional imaging with highly sparse sampling.

XI. CONCLUSIONS AND DISCUSSION

Here, we compressed the massive system in 3D PACT using spatiotemporal SVD and temporal FFT. On the basis of the compression, we proposed a hybrid method for fast functional imaging by using a prior image to manipulate the system matrix in sparse sampling. In both numerical simulations and mouse brain functional imaging *in vivo*, the hybrid method substantially mitigates artifacts in the reconstructed images and reduces false positive regions in the functional image, and its linearity is important for maintaining the true functional region. Due to its high robustness, the method can accelerate or enhance the performance of an existing system and reduce the cost of a future system for functional imaging.

It needs to be noted that the availability of the functional signal profile in this study allows us to use the highly robust correlation-based method for voxel-wise functional signal extraction. In studies where the profile is not available, other

types of functional signal extraction methods (e.g., bandpass filtering) can be used.

Although we demonstrated the system matrix compression and manipulation methods using only PACT, they are applicable to CT and MRI. System matrices in 3D PACT and CT correspond to sphere [10] and line [6] integrals, respectively, and the latter can be transformed using Grangeat's method [39] into plane integrals, which are locally equivalent to sphere integrals. System matrices in 2D PACT and CT [5] correspond to circle (reduced from a sphere) and line integrals, respectively, which are locally equivalent. MRI is more complex due to its high flexibility in k-space sampling. For radial-sampling MRI [30], [40], the acquired signals can be transformed to integrals on lines and planes, respectively, for 2D and 3D imaging using the Fourier slice theorem. For other sampling patterns, further analysis may disclose proper transformations to obtain integrals that are locally equivalent to those in PACT.

APPENDIX A

RECONSTRUCTIONS OF THE NUMERICAL PHANTOM (SHOWN IN

Fig. 3a) with K = 3 for D_1 , D_2 , D_3 , and D_4

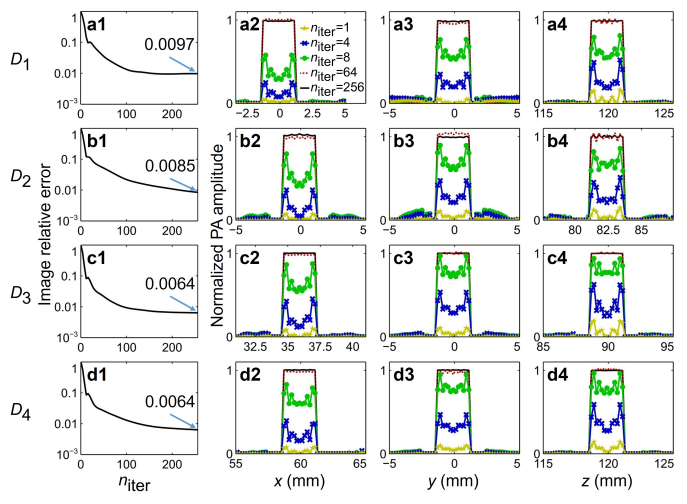


Fig. 8 Reconstructions of the numerical phantom (shown in Fig. 3a) with K = 3 for D_1 , D_2 , D_3 , and D_4 . a1 Relative error of the reconstructed image in the subdomain D_1 with 1 to 256 FISTA iterations. a2-a4 Values on the lines L1, L2, and L3 (shown in Fig. 3a), respectively, in the reconstructed images with $n_{\text{iter}} = 1, 4, 8, 64, 256$. b1-b4, c1-c4, and d1-d4 The same analysis for reconstructions in subdomains D_2 , D_3 , and D_4 , respectively.

APPENDIX B

SIMULATIONS FOR TWO COMPLEX NUMERICAL PHANTOMS

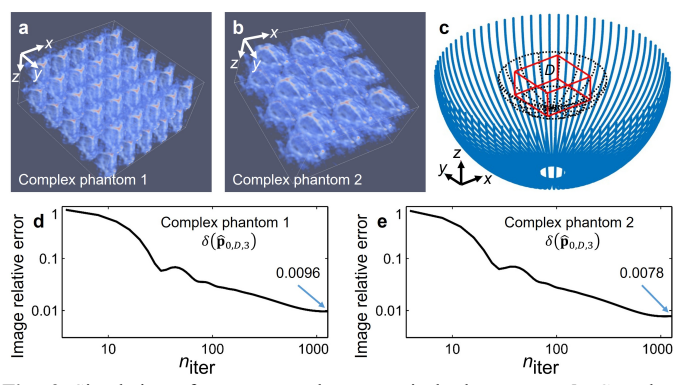


Fig. 9 Simulations for two complex numerical phantoms. **a-b** Complex numerical phantoms 1 and 2, respectively. **c** A virtual 2D array (blue-solid arcs), an image domain of size $6 \times 6 \times 3$ cm³ (D, red-solid box), and the black-dotted circles and arcs from **Fig. 3b. d-e** Relative error of the reconstructed image (4 to 1280 FISTA iterations) for the two numerical phantoms, respectively.

APPENDIX C

FUNCTIONAL SIGNALS IN THE MODULATED UBP AND

RESIDUAL UBP IMAGES

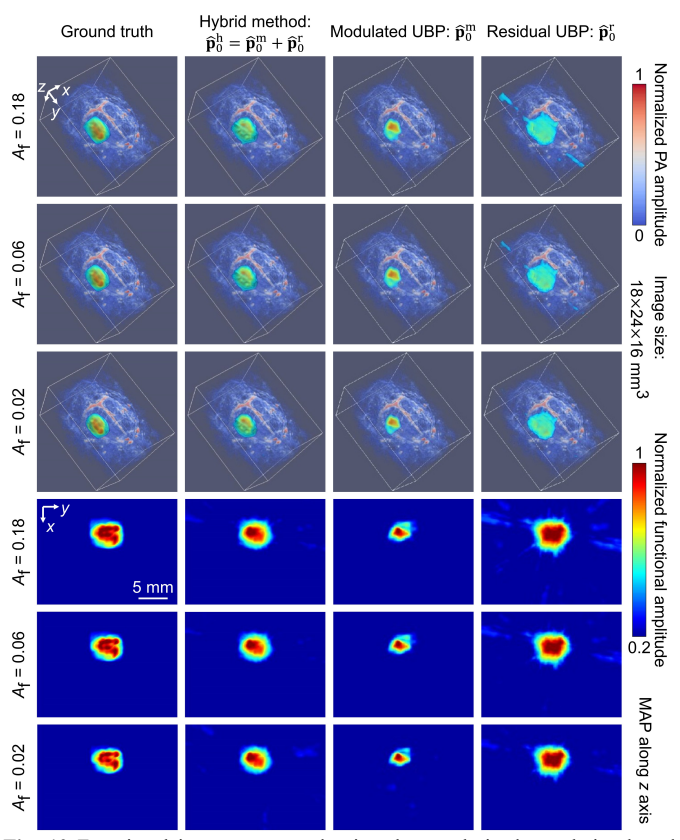


Fig. 10 Functional images extracted using the regularized-correlation-based method with $\lambda_f = 1.6$ from ground-truth images, hybrid images ($\hat{\mathbf{p}}_0^h = \hat{\mathbf{p}}_0^m + \hat{\mathbf{p}}_0^r$), modulated UBP images ($\hat{\mathbf{p}}_0^m$), and residual UBP images ($\hat{\mathbf{p}}_0^r$) for $A_f = 0.18, 0.06, 0.02$. Functional signals exist in both the modulated UBP images and the residual UBP images, and the signals are complementary.

REFERENCES

- [1] J. Hsieh, Computed Tomography: Principles, Design, Artifacts, and Recent Advances. SPIE Press, 2003.
- [2] Z.-P. Liang and P. C. Lauterbur, *Principles of magnetic resonance imaging*. SPIE Optical Engineering Press Bellingham, 2000.

- [3] R. B. Buxton, *Introduction to functional magnetic resonance imaging:* principles and techniques. Cambridge university press, 2009.
- [4] L. V. Wang and S. Hu, "Photoacoustic tomography: In vivo imaging from organelles to organs," *Science*, vol. 335, no. 6075, pp. 1458– 1462, 2012.
- [5] S. Zhang, D. Zhang, H. Gong, O. Ghasemalizadeh, G. Wang, and G. Cao, "Fast and accurate computation of system matrix for area integral model-based algebraic reconstruction technique," *Opt. Eng.*, vol. 53, no. 11, p. 113101, Nov. 2014.
- [6] G. Wang, M. W. Vannier, and P.-C. Cheng, "Iterative X-ray conebeam tomography for metal artifact reduction and local region reconstruction," *Microsc. Microanal.*, vol. 5, no. 1, pp. 58–65, Jan. 1999.
- [7] B. P. Sutton, D. C. Noll, and J. A. Fessler, "Fast, iterative image reconstruction for MRI in the presence of field inhomogeneities," *IEEE Trans. Med. Imaging*, vol. 22, no. 2, pp. 178–188, Feb. 2003.
- [8] J. A. Fessler, "Model-Based Image Reconstruction for MRI," *IEEE Signal Process. Mag.*, vol. 27, no. 4, pp. 81–89, Jul. 2010.
- [9] C. Huang, K. Wang, L. Nie, L. V. Wang, and M. A. Anastasio, "Full-wave iterative image reconstruction in photoacoustic tomography with acoustically inhomogeneous media," *IEEE Trans. Med. Imaging*, vol. 32, no. 6, pp. 1097–1110, Jun. 2013.
- [10] K. Wang, R. Su, A. A. Oraevsky, and M. A. Anastasio, "Investigation of iterative image reconstruction in three-dimensional optoacoustic tomography," *Phys. Med. Biol.*, vol. 57, no. 17, pp. 5399–5423, Sep. 2012.
- [11] S. Abbas, T. Lee, S. Shin, R. Lee, and S. Cho, "Effects of sparse sampling schemes on image quality in low-dose CT," *Med. Phys.*, vol. 40, no. 11, p. 111915, 2013.
- [12] M. Lustig, D. L. Donoho, J. M. Santos, and J. M. Pauly, "Compressed sensing MRI," *IEEE Signal Process. Mag.*, vol. 25, no. 2, pp. 72–82, Mar. 2008.
- [13] J. Provost and F. Lesage, "The application of compressed sensing for photo-acoustic tomography," *IEEE Trans. Med. Imaging*, vol. 28, no. 4, pp. 585–594, Apr. 2009.
- [14] T. Küstner, K. Armanious, J. Yang, B. Yang, F. Schick, and S. Gatidis, "Retrospective correction of motion-affected MR images using deep learning frameworks," *Magn. Reson. Med.*, vol. 82, no. 4, pp. 1527–1540, 2019.
- [15] Q. Lyu, H. Shan, Y. Xie, A. C. Kwan, Y. Otaki, K. Kuronuma, D. Li, and G. Wang, "Cine cardiac MRI motion artifact reduction using a recurrent neural network," *IEEE Trans. Med. Imaging*, vol. 40, no. 8, pp. 2170–2181, Aug. 2021.
- [16] G.-H. Chen, J. Tang, and S. Leng, "Prior image constrained compressed sensing (PICCS): A method to accurately reconstruct dynamic CT images from highly undersampled projection data sets," *Med. Phys.*, vol. 35, no. 2, pp. 660–663, 2008.
- [17] H. Yu and G. Wang, "SART-type image reconstruction from a limited number of projections with the sparsity constraint," *J. Biomed. Imaging*, vol. 2010, p. 3:1-3:9, Jan. 2010.
- [18] N. Davoudi, X. L. Deán-Ben, and D. Razansky, "Deep learning optoacoustic tomography with sparse data," *Nat. Mach. Intell.*, vol. 1, no. 10, pp. 453–460, Oct. 2019.
- [19] J. He, Q. Liu, A. G. Christodoulou, C. Ma, F. Lam, and Z.-P. Liang, "Accelerated high-dimensional MR imaging with sparse sampling using low-rank tensors," *IEEE Trans. Med. Imaging*, vol. 35, no. 9, pp. 2119–2129, 2016.
- [20] B. Zhao, W. Lu, T. K. Hitchens, F. Lam, C. Ho, and Z.-P. Liang, "Accelerated MR parameter mapping with low-rank and sparsity constraints," *Magn. Reson. Med.*, vol. 74, no. 2, pp. 489–498, 2015.
- [21] R. Otazo, E. Candes, and D. K. Sodickson, "Low-rank plus sparse matrix decomposition for accelerated dynamic MRI with separation of background and dynamic components," *Magn. Reson. Med.*, vol. 73, no. 3, pp. 1125–1136, 2015.
- [22] M. Akçakaya, S. Moeller, S. Weingärtner, and K. Uğurbil, "Scan-specific robust artificial-neural-networks for k-space interpolation (RAKI) reconstruction: Database-free deep learning for fast imaging," *Magn. Reson. Med.*, vol. 81, no. 1, pp. 439–453, 2019.
- [23] Y. Han, L. Sunwoo, and J. C. Ye, "k-space deep learning for accelerated MRI," *IEEE Trans. Med. Imaging*, vol. 39, no. 2, pp. 377– 386, Feb. 2020.
- [24] S. Winkelmann, T. Schaeffter, T. Koehler, H. Eggers, and O. Doessel, "An optimal radial profile order based on the golden ratio for time-

- resolved MRI," *IEEE Trans. Med. Imaging*, vol. 26, no. 1, pp. 68–76, Jan. 2007.
- [25] H. Lee, J. Lee, H. Kim, B. Cho, and S. Cho, "Deep-neural-network-based sinogram synthesis for sparse-view CT image reconstruction," *IEEE Trans. Radiat. Plasma Med. Sci.*, vol. 3, no. 2, pp. 109–119, Mar. 2019.
- [26] P. Hu, L. Li, L. Lin, and L. V. Wang, "Spatiotemporal Antialiasing in Photoacoustic Computed Tomography," *IEEE Trans. Med. Imaging*, vol. 39, no. 11, pp. 3535–3547, 2020.
- [27] C. Rohkohl, H. Bruder, K. Stierstorfer, and T. Flohr, "Improving best-phase image quality in cardiac CT by motion correction with MAM optimization," *Med. Phys.*, vol. 40, no. 3, p. 031901, 2013.
- [28] Y. Liu, C. Ma, B. A. Clifford, F. Lam, C. L. Johnson, and Z.-P. Liang, "Improved low-rank filtering of magnetic resonance spectroscopic imaging data corrupted by noise and B_0 field inhomogeneity," *IEEE Trans. Biomed. Eng.*, vol. 63, no. 4, pp. 841–849, 2015.
- [29] B. Zhu, J. Z. Liu, S. F. Cauley, B. R. Rosen, and M. S. Rosen, "Image reconstruction by domain-transform manifold learning," *Nature*, vol. 555, no. 7697, pp. 487–492, Mar. 2018.
- [30] L. Feng, L. Axel, H. Chandarana, K. T. Block, D. K. Sodickson, and R. Otazo, "XD-GRASP: Golden-angle radial MRI with reconstruction of extra motion-state dimensions using compressed sensing," *Magn. Reson. Med.*, vol. 75, no. 2, pp. 775–788, 2016.
- [31] P. Han, R. Zhang, S. Wagner, Y. Xie, E. Cingolani, E. Marban, A. G. Christodoulou, and D. Li, "Electrocardiogram-less, free-breathing myocardial extracellular volume fraction mapping in small animals at high heart rates using motion-resolved cardiovascular magnetic resonance multitasking: A feasibility study in a heart failure with preserved ejection fraction rat model," *J. Cardiovasc. Magn. Reson.*, vol. 23, no. 1, p. 8, Feb. 2021.
- [32] W. Wu, D. Hu, C. Niu, H. Yu, V. Vardhanabhuti, and G. Wang, "DRONE: Dual-domain residual-based optimization network for sparse-view CT reconstruction," *IEEE Trans. Med. Imaging*, vol. 40, no. 11, pp. 3002–3014, Nov. 2021.
- [33] P. Hu, L. Li, and L. V. Wang, "Location-dependent spatiotemporal antialiasing in photoacoustic computed tomography," *IEEE Trans. Med. Imaging*, vol. 42, no. 4, pp. 1210–1224, Apr. 2023.
- [34] G. Yang, S. Yu, H. Dong, G. Slabaugh, P. L. Dragotti, X. Ye, F. Liu, S. Arridge, J. Keegan, Y. Guo, and others, "DAGAN: deep de-aliasing generative adversarial networks for fast compressed sensing MRI reconstruction," *IEEE Trans. Med. Imaging*, vol. 37, no. 6, pp. 1310– 1321, 2017.
- [35] L. V. Wang and H. Wu, Biomedical optics: Principles and imaging. John Wiley & Sons, 2012.
- [36] L. Lin, P. Hu, X. Tong, S. Na, R. Cao, X. Yuan, D. C. Garrett, J. Shi, K. Maslov, and L. V. Wang, "High-speed three-dimensional photoacoustic computed tomography for preclinical research and clinical translation," *Nat. Commun.*, vol. 12, no. 1, pp. 1–10, 2021.
- [37] A. Beck and M. Teboulle, "A fast iterative shrinkage-thresholding algorithm for linear inverse problems," SIAM J. Imaging Sci., vol. 2, no. 1, pp. 183–202, 2009.
- [38] M. Xu and L. V. Wang, "Universal back-projection algorithm for photoacoustic computed tomography," *Phys. Rev. E*, vol. 71, no. 1, p. 016706, Jan. 2005.
- [39] P. Grangeat, "Mathematical framework of cone beam 3D reconstruction via the first derivative of the radon transform," in *Mathematical Methods in Tomography*, Berlin, Heidelberg, 1991, pp. 66–97.
- [40] K. T. Block, M. Uecker, and J. Frahm, "Undersampled radial MRI with multiple coils. Iterative image reconstruction using a total variation constraint," *Magn. Reson. Med.*, vol. 57, no. 6, pp. 1086–1098, 2007